Quasiparticle bands and structural phase transition of iron from Gutzwiller density-functional theory

Tobias Schickling, Jörg Bünemann, and Florian Gebhard*
Fachbereich Physik, Philipps-Universität Marburg, D-35032 Marburg, Germany

Lilia Boeri
Institute for Theoretical and Computational Physics, TU Graz, A-8010 Graz, Austria
(Received 26 October 2015; revised manuscript received 9 April 2016; published 26 May 2016)

We use the Gutzwiller density-functional theory to calculate ground-state properties and band structures of iron in its body-centered-cubic (bcc) and hexagonal-close-packed (hcp) phases. For a Hubbard interaction $U = 9$ eV and Hund's-rule coupling $J = 0.54$ eV, we reproduce the lattice parameter, magnetic moment, and bulk modulus of bcc iron. For these parameters, bcc is the ground-state lattice structure at ambient pressure up to a pressure of $p_c = 41$ GPa where a transition to the nonmagnetic hcp structure is predicted, in qualitative agreement with experiment ($p_c^{\rm exp} = 10, \ldots, 15$ GPa). The calculated band structure for bcc iron is in good agreement with ARPES measurements. The agreement improves when we perturbatively include the spin-orbit coupling.

DOI: 10.1103/PhysRevB.93.205151

I. INTRODUCTION

The theoretical description of the structural and electronic properties of iron poses an interesting but difficult problem. Since iron is an essential element in the inner core of the earth, it is desirable to know its phase diagram over a wide temperature and pressure range. However, basic calculations at ambient pressure and zero temperature reveal the intricacy of the iron problem. *Ab initio* calculations with density-functional theory (DFT) in the local density approximation, DFT(LDA), predict a wrong lattice structure for the ground state, namely face-centered-cubic (fcc) or hexagonal-close-packed (hcp) [1,2]. Employing DFT with a generalized gradient approximation, DFT(GGA), standard band structure theory recovers the experimentally observed ferromagnetic body-centered-cubic (bcc) structure and the bcc-hcp transition [3,4]. Using the standard GGA functional of Perdew, Burke, and Ernzerhof (PBE) [5], a good description of the lattice parameter, magnetization, and compressibility of iron, cobalt, and nickel is obtained [6,7]. However, as for nickel [8], both DFT functionals lead to a d-electron bandwidth that is too large and quasiparticle masses at the Fermi edge that are too small in comparison with experiment [9]. This indicates that neither of the DFT functionals takes into account the correlations among the $3d$ electrons in an optimal way.

Coulomb correlations for electrons in narrow bands are often modeled by a purely local, Hubbard-type interaction [10–13]. Typically, the effective atomic interactions are parameterized by an intra-orbital Hubbard interaction U and a Hund's-rule coupling J. Unfortunately, Hubbard models pose a notoriously difficult many-body problem.

Over the past three decades, two many-body approaches emerged that permit a treatment of Hubbard-type interactions in the limit of infinite lattice coordination number in combination with DFT. First, the dynamical mean-field theory (DMFT) [14,15] maps the problem onto a single-impurity model. The spectral function of the (multi-orbital) single-impurity model is calculated numerically, typically using the quantum Monte-Carlo method [16]. With DMFT(QMC), iron's structural and magnetic transitions at temperatures $T > 1000$ K were studied in Ref. [17] (and references therein), and the equation-of-state for the bcc-hcp phase transition was investigated in Ref. [18]. Second, the Gutzwiller many-body wave function is combined with DFT(LDA) to treat local interactions variationally ("LDA+Gutzwiller," "Gutzwiller-DFT"), see Refs. [8,19–32]. Recently, the LDA+Gutzwiller approach was applied to a number of transition metals including nickel, iron, and iron pnictides. [21,23,25,33,34]

The DMFT becomes exact in infinite dimensions but the numerical effort is quite considerable, which often makes further simplifications of the interactions advisable [17]. Moreover, the computational demands limit the studies to elevated temperatures and prohibits an extensive scan in the (U, J) parameter space. On the other hand, the Gutzwiller approach is a variational method at zero temperature and therefore best suited for the calculation of ground-state properties such as the lattice parameter, magnetization, and bulk modulus. Dynamical properties, however, can only be described within the quasiparticle picture, i.e., the method provides a band structure but no quasiparticle lifetimes. Since the Gutzwiller-DFT is computationally much cheaper than DFT(LDA-DMFT), it permits a survey of the (U, J) parameter space for iron.

In this study, we present comprehensive results for iron obtained from the LDA+Gutzwiller method. We obtain the experimental values for the lattice parameter, magnetization, and compressibility, and provide a qualitatively correct description of the structural transition from bcc to hcp iron under pressure. When we take spin-orbit effects into account perturbatively, we obtain a good agreement with ARPES measurements of the quasiparticle band structure [35].

Our work is structured as follows. In Sec. II, we summarize the Gutzwiller-DFT that was derived in detail in Ref. [8]; here, we generalize it to the case of more than one atom per unit cell. In Sec. III we discuss our results for the ground-state properties of iron. In Sec. IV, we present the respective quasiparticle band structures and compare them to ARPES data for bcc iron. Conclusions, Sec. V, close our presentation.

*florian.gebhard@physik.uni-marburg.de

II. METHOD

The Gutzwiller-DFT and the minimization algorithm, which we use in this work have been discussed in detail in Refs. [8,36]. Therefore we will only summarize the main ideas of these methods in the present section and focus on some particular aspects that are relevant in our calculations for iron.

A. Gutzwiller-DFT

Instead of a single-particle reference system that leads to the standard Kohn-Sham equations, the Gutzwiller-DFT employs a many-particle reference system. It explicitly takes into account the local Coulomb interaction (on lattice sites $\mathbf{R}$)

$$\hat{V}_{\mathrm{loc}} = \sum_{\mathbf{R}} \hat{V}_{\mathrm{loc}}(\mathbf{R}), \tag{1}$$

$$\hat{V}_{\mathrm{loc}}(\mathbf{R}) = \sum_{\gamma_1,\ldots,\gamma_4} U^{\gamma_1,\gamma_2}_{\gamma_3,\gamma_4}\, \hat{c}^{+}_{\mathbf{R},\gamma_1} \hat{c}^{+}_{\mathbf{R},\gamma_2} \hat{c}_{\mathbf{R},\gamma_3} \hat{c}_{\mathbf{R},\gamma_4} \tag{2}$$

in those spin-orbital states $\phi_{\mathbf{R},\gamma}(\mathbf{r}) \equiv \phi_{\mathbf{R},c,\sigma}(\mathbf{r})$ which are deemed to be strongly correlated. In our iron calculations, these are the e_g and t_{2g} orbitals of the $3d$ shell. The explicit form of the operator $\hat{V}_{\mathrm{loc}}(\mathbf{R})$ for d orbitals is given in Ref. [8], see also Appendix. As also shown in that work, one obtains the following "Hubbard density functional" for the many-particle reference system:

$$\begin{aligned} E_{\mathrm{H}}[\{n_\sigma(\mathbf{r})\}] = {} & K_{\mathrm{H}}[\{n_\sigma(\mathbf{r})\}] + U[\{n_\sigma(\mathbf{r})\}] + V_{\mathrm{Har}}[\{n_\sigma(\mathbf{r})\}] \\ & + V_{\mathrm{loc}}[\{n_\sigma(\mathbf{r})\}] - V_{\mathrm{dc}}[\{n_\sigma(\mathbf{r})\}] \\ & + E_{\mathrm{H,xc}}[\{n_\sigma(\mathbf{r})\}], \end{aligned} \tag{3}$$

where $E_{\mathrm{H,xc}}[\{n_\sigma(\mathbf{r})\}]$ is the exchange-correlation functional, see Sec. II C, and

$$U[\{n_\sigma(\mathbf{r})\}] = \sum_{\sigma} \int d\mathbf{r} U(\mathbf{r}) n_\sigma(\mathbf{r}), \tag{4}$$

$$V_{\mathrm{Har}}[\{n_\sigma(\mathbf{r})\}] = \sum_{\sigma,\sigma'} \iint d\mathbf{r} d\mathbf{r}' V(\mathbf{r}-\mathbf{r}') n_\sigma(\mathbf{r}) n_{\sigma'}(\mathbf{r}'), \tag{5}$$

$$K_{\mathrm{H}}[\{n_\sigma(\mathbf{r})\}] = \left\langle \Psi^{(n)}_{\mathrm{H},0} \middle| \hat{H}_{\mathrm{kin}} \middle| \Psi^{(n)}_{\mathrm{H},0} \right\rangle, \tag{6}$$

$$V_{\mathrm{loc/dc}}[\{n_\sigma(\mathbf{r})\}] = \left\langle \Psi^{(n)}_{\mathrm{H},0} \middle| \hat{V}_{\mathrm{loc/dc}} \middle| \Psi^{(n)}_{\mathrm{H},0} \right\rangle. \tag{7}$$

Here, we introduced the periodic potential $U(\mathbf{r})$ of the nuclei and the two-particle Coulomb interaction $V(\mathbf{r}-\mathbf{r}')$. The state $|\Psi^{(n)}_{\mathrm{H},0}\rangle$ minimizes, by definition, the expectation value of the Hamiltonian

$$\hat{H}_{\mathrm{H}} = \hat{H}_{\mathrm{kin}} + \hat{V}_{\mathrm{loc}} - \hat{V}_{\mathrm{dc}}, \tag{8}$$

for a given (and fixed) particle density $n_\sigma(\mathbf{r})$. Finally, the "double-counting operator" $\hat{V}_{\mathrm{dc}}$ and the corresponding functional $V_{\mathrm{dc}}[\{n_\sigma(\mathbf{r})\}]$ account for the fact that the local Coulomb interaction between electrons in the correlated orbitals is already included in the Hartree energy and the exchange-correlation functional. Unfortunately, there is no systematic way to derive $\hat{V}_{\mathrm{dc}}$ for a given local Hamiltonian $\hat{V}_{\mathrm{loc}}$. We work with the widely used form of the double-counting functional [14,21,37,38], see Appendix.

In contrast to the corresponding Kohn-Sham functional, $E_{\mathrm{H}}[\{n_\sigma(\mathbf{r})\}]$ cannot be minimized without further approximations. In fact, it cannot even be evaluated because $\hat{H}_{\mathrm{H}}$ is a many-particle Hamiltonian. We therefore use Gutzwiller wave functions for the evaluation of (6) and (7). They are defined as

$$|\Psi_{\mathrm{G}}\rangle = \hat{P}_{\mathrm{G}} |\psi_0\rangle, \tag{9}$$

$$\hat{P}_{\mathrm{G}} = \prod_{\mathbf{R}} \sum_{\Gamma,\Gamma'} \lambda_{\Gamma,\Gamma'}(\mathbf{R}) \hat{m}_{\mathbf{R};\Gamma,\Gamma'}, \tag{10}$$

where $|\psi_0\rangle$ is a single-particle product state, and $\lambda_{\Gamma,\Gamma'}(\mathbf{R})$ are the elements of the variational parameter matrix $\tilde{\lambda}(\mathbf{R})$. We further introduced the eigenstates $|\Gamma\rangle_{\mathbf{R}}$ of $\hat{V}_{\mathrm{loc}}(\mathbf{R})$ and the operator

$$\hat{m}_{\mathbf{R};\Gamma,\Gamma'} \equiv |\Gamma\rangle_{\mathbf{R}\mathbf{R}} \langle \Gamma'|. \tag{11}$$

In our calculations for iron, we work with a diagonal and lattice-site independent variational parameter matrix $\lambda_{\Gamma,\Gamma'}(\mathbf{R}) = \delta_{\Gamma,\Gamma'}\lambda_\Gamma$, i.e., our energy functional depends on $n_\Gamma = 2^{10} = 1024$ variational parameters λ_Γ. Note that nondiagonal variational parameters do not substantially change the results in our high-symmetry cubic situation in the absence of spin-orbit coupling. Moreover, we do not find it necessary to implement symmetry relations among the 1024 variational parameters. This has been done in Ref. [33] where also nondiagonal variational parameters $\lambda_{\Gamma,\Gamma'}$ were taken into account.

The evaluation of Eqs. (6) and (7) still is a difficult many-particle problem. It can be solved in the limit of infinite spatial dimensions where one obtains an analytical energy functional. Using this energy functional in calculations on finite-dimensional systems, as done in this work, is usually denoted as the "Gutzwiller approximation" to the energy functional $E_{\mathrm{H}}[\{n_\sigma(\mathbf{r})\}]$.

We shall not repeat here the details of the Gutzwiller approximation or the structure of the resulting energy functional because it has been thoroughly discussed in earlier work. Obviously, one obtains a functional of the form

$$E_{\mathrm{H}} = E_{\mathrm{H}}(|\psi_0\rangle, \{\lambda_\Gamma\}) \tag{12}$$

that depends on the single-particle state $|\psi_0\rangle$ and the variational parameters λ_Γ. The minimization of the energy functional with respect to $|\psi_0\rangle$ leads to an effective single-particle Schrödinger equation for $|\psi_0\rangle$. This "Gutzwiller-Kohn-Sham equation" is the equivalent to the Kohn-Sham equation in ordinary DFT calculations and is solved by an adapted version of the open source QUANTUM ESPRESSO code [39].

For the minimization with respect to the variational parameters λ_Γ ("inner minimization"), we use an algorithm whose elements were discussed in Ref. [36]. The new feature of our present calculations comes from the fact that in hcp iron we have a unit cell with two iron atoms. Since both iron sites have the same point symmetry one could actually use the existing minimization algorithm [36]. For later use and testing purposes, however, we developed a code that is capable to carry out the inner minimization for a large number of in-equivalent correlated atoms per unit cell. We explain this algorithm in the following Sec. II B.

B. Inner minimization for systems with multiple atoms per unit cell

Let $l = 1, \ldots, n_l$ be the label for the n_l atoms in the unit cell and $\tilde{\lambda}^l$ the corresponding matrices of variational parameters. Then, for a translationally invariant system, the energy functional of the Gutzwiller approximation has the form

$$E(\{\tilde{\lambda}^l\}) = \sum_l V_{l;\mathrm{loc}}(\tilde{\lambda}^l) + \sum_l \sum_{\gamma_1,\gamma_2} q^{l;\gamma_2}_{\gamma_1}(\tilde{\lambda}^l) K^l_{\gamma_1,\gamma_2} + \mathrm{c.c.} + \sum_{l,l'} \sum_{\gamma_1,\ldots,\gamma_4} q^{l;\gamma_2}_{\gamma_1}(\tilde{\lambda}^l)(q^{l';\gamma_4}_{\gamma_3}(\tilde{\lambda}^{l'}))^* I^{l,l'}_{\gamma_1,\gamma_2,\gamma_3,\gamma_4}. \quad (13)$$

The third line describes the hopping of electrons between correlated orbitals, while the second line includes all contributions from hopping processes into noncorrelated orbitals. During the inner minimization, the tensors $K^l_{\gamma_1,\gamma_2}$ and $I^{l,l'}_{\gamma_1,\gamma_2,\gamma_3,\gamma_4}$ are just numbers that result from the solution of the Gutzwiller–Kohn-Sham equation. Note that in our calculations for iron, the renormalization matrices $q^{l;\gamma_2}_{\gamma_1}$ are real and diagonal, $q^{l;\gamma_2}_{\gamma_1} = \delta_{\gamma_1,\gamma_2} q^{l;\gamma_1}_{\gamma_1}$, which simplifies the energy functional considerably.

The energy functional (13) needs to be minimized with respect to all matrices $\tilde{\lambda}^l$. Even with our diagonal Ansatz for $\tilde{\lambda}^l$, however, the total number of variational parameters $n_{\mathrm{tot}} = n_\Gamma \times n_l$ would become prohibitively large if we tried to minimize straightforwardly systems with different atoms in the unit cell. Instead of minimizing (13) directly with respect to all matrices $\tilde{\lambda}^l$ simultaneously, we therefore use the following scheme. (i) Start with some initial values for the matrices $\tilde{\lambda}^l_0$ and the corresponding renormalization matrices $q^{l;\gamma_2}_{\gamma_1;0} \equiv q^{l;\gamma_2}_{\gamma_1}(\tilde{\lambda}^l_0)$, e.g., the values in the noninteracting limit. (ii) Minimize the n_l individual energy functionals

$$E_l(\tilde{\lambda}^l) = V_{l;\mathrm{loc}}(\tilde{\lambda}^l) + \sum_{\gamma_1,\gamma_2} q^{l;\gamma_2}_{\gamma_1}(\tilde{\lambda}^l) K^l_{\gamma_1,\gamma_2} + \mathrm{c.c.} + \frac{1}{2} \sum_{l'} \sum_{\gamma_1,\ldots,\gamma_4} q^{l;\gamma_2}_{\gamma_1}(\tilde{\lambda}^l)\left(q^{l';\gamma_4}_{\gamma_3;0}\right)^* I^{l,l'}_{\gamma_1,\gamma_2,\gamma_3,\gamma_4} \quad (14)$$

with respect to $\tilde{\lambda}^l$, e.g., by means of the algorithm introduced in Ref. [36]. (iii) If the matrices $\tilde{\lambda}^l_1$ minimize the n_l functionals (14), set $\tilde{\lambda}^l_0 = \tilde{\lambda}^l_1$ and go back to step (i) until a converged solution has been reached.

In our actual calculations, the band optimization (Gutzwiller-Kohn-Sham equations for $|\psi_0\rangle$) and of the local parameters (inner minimization) are not separated. After an update of the matrices $\tilde{\lambda}^l$ in step (ii), the matrices $q^{l;\gamma_2}_{\gamma_1}$ are recalculated. Then, the Gutzwiller-Kohn-Sham equation is solved again to arrive at new values for the tensors $K^l_{\gamma_1,\gamma_2}$ and $I^{l,l'}_{\gamma_1,\gamma_2,\gamma_3,\gamma_4}$ in Eq. (14). Typically, we need 10 to 15 iterations of the combined cycle of band optimization and inner minimization to reach a converged minimum.

C. Computational details

Our work is based on the open-source plane-wave pseudopotential code QUANTUM ESPRESSO [39]. We implemented the routines necessary for the Gutzwiller-DFT, as described previously in Ref. [8], see the supplemental material for further information [40]. For the Gutzwiller-Kohn-Sham calculations we used the LDA exchange-correlation functional of Perdew and Zunger for $E_{\mathrm{H,xc}}[\{n_\sigma(\mathbf{r})\}]$; note that our calculations start from the local spin-density approximation (LSDA) so that we recover the results from DFT(LSDA) for $U = J = 0$. For comparison, we also performed GGA calculations based on the Perdew-Burke-Ernzerhof functional. To model the electron-core interaction, we employed ultrasoft pseudopotentials from the standard QUANTUM ESPRESSO distribution with nonlinear core corrections. These are Fe.pz-nd-rrkjus.UPF (LDA), and Fe.pbe-spn-rrkjus$_{\mathrm{p}}$sl.0.2.1.UPF (Fe.rel-pbe-spn-rrkjus$_{\mathrm{p}}$sl.0.2.1.UPF) for (scalar) relativistic GGA calculations. The GGA pseudopotentials yield equilibrium lattice constants ($a_{\mathrm{GGA}} = 5.39 a_{\mathrm{B}}$), magnetic moments ($m_{\mathrm{GGA}} = 2.25 \mu_B$), and electronic structure in excellent agreement with previous full-potential calculations [35].

In Gutzwiller-DFT, we find that a very accurate integration over $\mathbf{k}$ space is needed for a proper convergence. Therefore integrations over the Brillouin zone are performed using the tetrahedron method. For bcc iron, we use at least 624 $\mathbf{k}$ points in the irreducible part of the Brillouin zone. For nonmagnetic hcp, we work with 729 inequivalent $\mathbf{k}$ points. For all calculations a wave cutoff of 60 Ry was set, and a charge-density cutoff of 600 Ry.

For the construction of the $3d$ orbitals, we employ the program package POORMANWANNIER that is part of the standard QUANTUM ESPRESSO distribution. We generate Wannier functions using a very large energy window of 90 eV around the Fermi energy and the resulting $3d$ orbitals are very close to localized $3d$ orbitals. More details on the choice of the energy window and implementations are given in Sec. III A in Ref. [40]. In the following, we denote our implementation of the LDA+Gutzwiller scheme as "Gutzwiller-DFT."

III. GROUND-STATE PROPERTIES

A. Adjustment of the Coulomb parameters

The Gutzwiller-DFT is not a fully *ab initio* method. The Coulomb interaction between the $3d$ electrons is parameterized by the Hubbard interaction U and the Hund's-rule coupling J. In this work, we choose to adjust these two parameters such that the Gutzwiller-DFT reproduces the experimental values for the lattice parameter a and the magnetization m; see our discussion Sec. III A 3.

The DFT(LDA) predicts an fcc or hcp crystal structure as the ground state for iron at ambient pressure [1,2]. Therefore we do not show the results for $U = J = 0$ in the following. This serious flaw of DFT(LDA) is easily overcome with LDA+Gutzwiller, and also in DFT(GGA) where $a_{\mathrm{GGA}} \approx 5.36\, a_{\mathrm{B}}$ and $m \approx 2.2\, \mu_{\mathrm{B}}$ are obtained [3,4]. For local interactions as small as $U \geqslant 1.0$ eV and $J = 0.06U$, Gutzwiller-DFT finds the experimentally observed ferromagnetic bcc lattice structure. Therefore the correct ground-state structure dominates the (U, J) phase diagram, and it is straightforward to search for the optimal Hubbard interaction U and Hund's-rule coupling J, as was done for nickel previously [8].

1. *Lattice parameter*

In Fig. 1, we display the bcc lattice parameter $a(U, J)$ as a function of U for various ratios J/U. The horizontal dashed

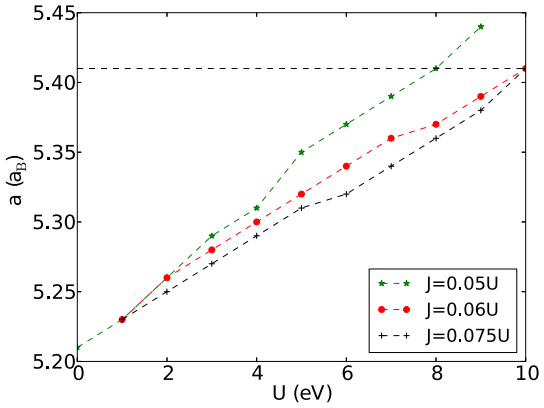

FIG. 1. Cubic lattice parameter $a(U,J)$ for bcc iron in units of the Bohr radius $a_B = 0.529$ Å as a function of the Hubbard interaction U for $J/U = 0.05,\ 0.06$, and 0.075. The horizontal dashed line indicates the experimental value $a^{exp} = 5.42a_B = 2.87$ Å.

line indicates the experimental value, $a^{exp} = 5.42a_B = 2.87$ Å [41]. As also seen in nickel [8], the lattice parameter increases monotonously as a function of the Hubbard interaction. This effect is desired because the DFT(LDA) considerably underestimates the lattice parameter for iron.

The influence of the Hubbard interaction is readily understood. The Coulomb repulsion weakens the contribution of the $3d$ electrons to the metallic binding so that the crystal is less tightly bound; the crystal volume increases as a function of the Coulomb repulsion. Figure 1 shows that the Hund's-rule coupling J counteracts the Hubbard interaction U. The slope of $a(U,J)$ as a function of U becomes smaller for larger J. This indicates that the Hund's-rule coupling J in iron has a tendency to increase the electrons' itineracy, see below.

2. Magnetization

In Fig. 2, we show the ordered magnetic moment $m(U,J)$ as a function of the Hubbard interaction U for the previously used ratios $J/U = 0.05,0.06,0.075$. The horizontal dashed line indicates the experimental value, $m^{exp} = 2.22\mu_B$ [42]. The

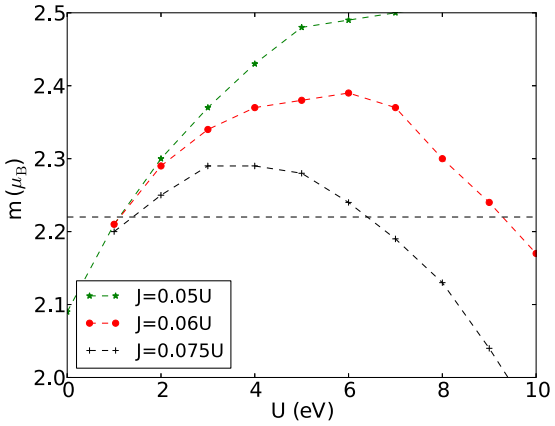

FIG. 2. Magnetization $m(U,J)$ in units of Bohr magneton μ_B as a function of the Hubbard interaction U for $J/U = 0.05,\ 0.06$, and 0.075. The horizontal dashed line indicates the experimental value $m = 2.22\mu_B$.

ordered magnetic moment m is calculated from the particle densities $n_\sigma(\mathbf{r})$ as

$$m/\mu_B = \int d\mathbf{r}[n_\uparrow(\mathbf{r}) - n_\downarrow(\mathbf{r})]\,, \tag{15}$$

where we used $g = 2$ as the electrons' gyromagnetic factor.

It is important to note that the DFT(LDA) predicts a large magnetization, i.e., iron is a band ferromagnet in DFT(LSDA). Figure 2 shows that the Coulomb corrections due to the intra-atomic correlations in the $3d$ shell amount to only 10% of the magnetization. Indeed, in the parameter regime shown in Fig. 2, we have $2.0\mu_B < m < 2.4\mu_B$ for 1 eV $\leqslant U \leqslant$ 9 eV and $J/U = 0.06$ and 0.075.

Since the Coulomb correlations in the $3d$ shell are not the primary cause for magnetism, the magnetization $m(U,J)$ does not show a simple dependence on the Hubbard interaction U in combination with the Hund's-rule coupling J. In iron, for vanishing Hund's-rule coupling, $J/U = 0$, we find that the magnetization increases as a function of U, as also seen in LDA+U. This is the usual Stoner mechanism: in a magnetized system there is less Coulomb energy to be paid, at the price of a loss in kinetic energy. When we increase U, the energy balance is shifted towards the exchange-energy gain so that the magnetization increases.

Within the Gutzwiller-DFT, the Hund's-rule coupling leads to the rather unexpected behavior seen in Fig. 2. For fixed U, an *increase* of the Hund's-rule coupling J leads to a *decrease* of the magnetization $m(U,J)$. Such a behavior was observed previously in iron [21], and also in nickel [8]. Moreover, the influence of the Hund's-rule coupling is not small. Indeed, as seen in Fig. 2, it leads to a parabolic downturn of $m(U,J)$ as a function of U for fixed J/U. We shall discuss the effect of the Hund's-rule coupling in more detail in Sec. III B 3.

Using the information in Figs. 1 and 2 we can determine the optimal values for the interaction parameters. For $U_{opt} = 9.0$ eV and $J_{opt} = 0.54$ eV, we obtain good results for the lattice parameter and the magnetic moment, $a_{opt} = a(U_{opt},J_{opt}) = 5.39a_B = 2.85$ Å and $m_{opt} = m(U_{opt},J_{opt}) = 2.24\mu_B$, that agree very well with the experimental values. In the rest of paper, we refer to the parameter set (U_{opt},J_{opt}) as our "optimal" atomic parameters.

3. Size of optimal atomic parameters

Before we proceed, we briefly comment on our optimal Coulomb parameters because they are substantially larger than parameters used in other studies for iron [17,43–46]. In most previous studies, the values $U = 2,\ldots,3$ eV and $J = 0.8,\ldots,1.0$ eV are used, e.g., to describe the high-temperature regime with the transition from fcc iron to bcc iron and the Curie transition from nonmagnetic to magnetic bcc iron, while more recent LDA+DMFT studies employ larger values, $\bar{U} = 4.3$ eV and $\widetilde{J} = 1.0$ eV [18]. In all cases, the explored parameter regime appears to be quite different from ours.

First of all, we note that the large spread of values of (U,J) in the literature is due to the strong sensitivity of these parameters to the energy window used for projecting, or downfolding, the full electronic structure to an effective many-body model [47]. It is well known that the bare Hubbard parameters U are of the order of 20 eV, or larger [10]. They

apply for instantaneous charge excitations of an isolated atom, which are strongly screened in a solid. In Fe, for example, the screening reduces U to ~ 3 eV for d-only models [34,48]. Our self-consistent DFT method is based on a projective technique to construct Wannier functions. In the present calculations, we chose a large energy window, which ensures a very good localization of the Fe $3d$ orbitals, and a minimal dependence of the basis set on atomic positions. This large energy window translates into larger values of U and J [49]. Other calculations can typically afford to retain fewer bands.

Second, we note that the Hubbard-U in our treatment parameterizes the interaction of two electrons in the same orbital, see Appendix. In other approaches, this quantity describes some orbital average. For example, Pourovskii *et al.* [18] use the Slater-Condon parameter $F^{(0)} = \bar{U}$, where $\bar{U} = (U + 4U')/5$, see Eq. (A9), and $U' = A - B + C = U - 2J$ is the interorbital Coulomb repulsion. Naturally, the intra-orbital U is larger than an average over intraorbital and interorbital Coulomb repulsions. Likewise, we work with the average Hund's-rule coupling $J = 5B/2 + C$, see Eq. (A6), whereas $\tilde{J} \equiv (F^{(2)} + F^{(4)})/14 = 7B/2 + 7C/5 = 7J/5$ [18]. Therefore $F^{(0)} = 4.3$ eV and $\tilde{J} = 1.0$ eV correspond to $J = 0.71$ eV and $U = \bar{U} + 8\tilde{J}/7 = 5.4$ eV with $J/U = 0.13$. We note in passing that we work with $C/B = 4$, whereas others use $F^{(2)}/F^{(4)} = 8/5$, which corresponds to $C/B = 175/47 \approx 3.7$ [50].

Lastly, in our Gutzwiller calculations, we use parameters such as U and J to "match" selected experimental quantities. In this way, we compensate approximations in the model setup, e.g., the neglect of nonlocal correlations in Hubbard-type models, and in the model analysis, e.g., the limit of infinite dimensions or an approximate variational ground state. For example, in Gutzwiller calculations, the optimal Coulomb parameters must be chosen somewhat smaller when the full atomic interaction is replaced by density-density interactions only [34]. Similarly, larger U values are found to be optimal when the impurity solver in quantum Monte Carlo is rotationally invariant [17]. In the following, we will show that our optimal atomic parameters lead to a good agreement with experiment. In particular, our substantial Hubbard interaction leads to noticeable bandwidth renormalizations and an increase of the quasiparticle masses at the Fermi energy, as seen in experiment [35,51].

We note that the atomic parameters for our study of iron resemble those used in recent LDA+Gutzwiller studies by Deng *et al.* [20,21] and our results agree quite well; on the other hand, we do not agree with Borghi *et al.* [33] who advocate small Hubbard interactions in their LDA+Gutzwiller work; however, as discussed in the following, there are sizable discrepancy between their and our results already at the DFT(LDA) level, and this prevents a detailed comparison.

B. Physical properties within Gutzwiller-DFT

After fixing the parameters, we are in the position to test the Gutzwiller-DFT against independent experimental observations. Here, we choose the bulk modulus and the transition from ferromagnetic bcc iron to nonmagnetic hcp iron. Furthermore, we discuss the local occupancies in more detail to elucidate the unexpected effect of the Hund's-rule coupling on the magnetization seen in Fig. 2.

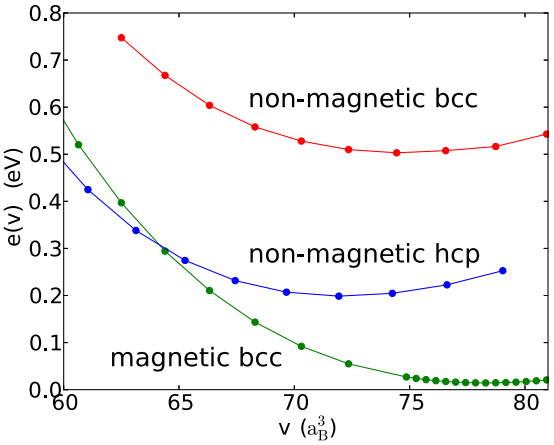

FIG. 3. Energy per atom $e(v)$ in units of eV as a function of the unit-cell volume v in units of a_B^3 for nonmagnetic and ferromagnetic bcc iron and nonmagnetic hcp iron at $U = 9$ eV and $J = 0.54$ eV and ambient pressure. The energies are shifted by the same constant amount.

1. Bulk modulus

In Fig. 3, we show the ground-state energy per atom, $e(v) = E(V)/N$, as a function of the unit-cell volume $v = V/N = a^3/2$ in the vicinity of the optimal value $v_0 = a_{\rm opt}^3/2 = 78.3a_B^3 = 11.6$ Å^3 with $a_{\rm opt} = 5.39a_B = 2.85$ Å. The bulk modulus at zero temperature is defined as the second-derivative of the ground-state energy $E(V)$ with respect to the volume,

$$B = v_0 \frac{d^2 e(v)}{dv^2}\bigg|_{v=v_0}. \tag{16}$$

This implies the Taylor expansion $e(v) = e(v_0) + (Bv_0/2)(v/v_0 - 1)^2 + \cdots$ for the ground-state energy (Birch-Murnaghan fit). Therefore we find the bulk modulus from the curvature of $e(v)$ near $v = v_0$.

In Gutzwiller-DFT we find a bulk modulus of $B = 165$ GPa, in very good agreement with the experimental value, $B^{\rm exp} = (170 \pm 4)$ GPa [41,52]. The LDA+Gutzwiller value substantially improves the DFT(LDA) value of $B^{\rm LDA} = 227$ GPa, it is slightly better than the values from DFT(GGA) studies, $B^{\rm GGA} = (190 \pm 10)$ GPa [41] and agrees with the value obtained in DMFT calculations, $B^{\rm DMFT} = 168$ GPa [18].

2. Pressure-induced transition from bcc to hcp iron

Figure 3 shows that the bcc structure is only stable because it is ferromagnetic [53]. By reducing the volume by applying external pressure, a first-order structural transition is observed at a pressure of $p_c^{\rm exp} = 10, \ldots, 15$ GPa at room temperature [54], together with the concomitant electronic and magnetic changes [9,55].

In Fig. 4, we plot the enthalpy difference per atom between the nonmagnetic hcp lattice and the ferromagnetic bcc lattice as a function of applied pressure for $U = 8.0$, 9.0 and 10 eV for fixed ratio $J/U = 0.06$. For our optimal parameter set ($U = 9.0$ eV and $J = 0.06U = 0.54$ eV), we obtain $p_c = 41$ GPa as

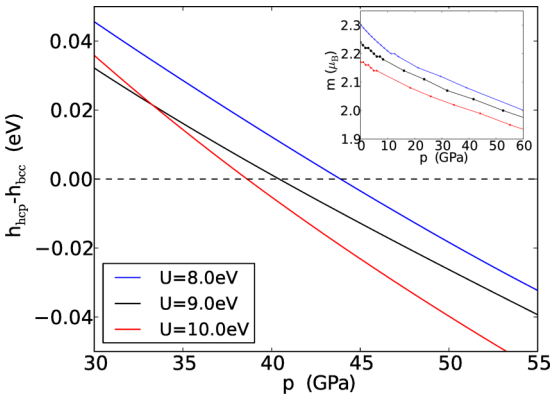

FIG. 4. Enthalpy difference per atom $h_{\rm hcp} - h_{\rm bcc}$ in units of eV between nonmagnetic hcp iron and ferromagnetic bcc iron as a function of applied pressure p for $U = 8.0,\ 9.0,\ 10$ eV and $J/U = 0.06$. Inset: magnetization as a function of pressure.

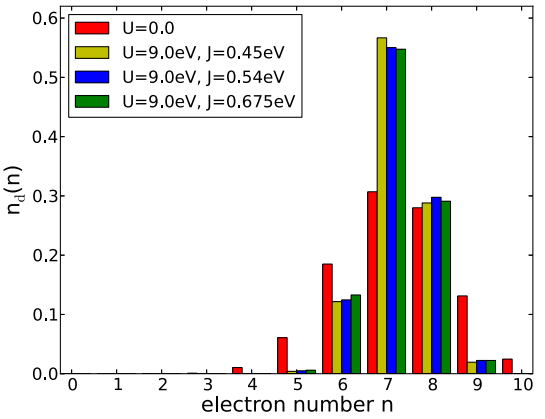

FIG. 5. Local charge distribution of iron atoms $n_d(n)$ for $U = 0$ (LDA limit) and $U = 9$ eV and $J/U = 0.05,\ 0.06$, and 0.075 (Gutzwiller-DFT) for optimal lattice parameters.

critical pressure at zero temperature, in qualitative agreement with experiment. The critical parameter only slightly depends on the value of U in the vicinity of $U = U_{\rm opt}$. We find at $J/U = 0.06$ that $p_{\rm c}$ decreases as a function of U, from $p_{\rm c} = 44$ GPa for $U = 8.0$ eV down to $p_{\rm c} = 38$ GPa for $U = 10$ eV. Therefore the transition at positive pressures is a robust feature in Gutzwiller-DFT. We note in passing that the critical pressure sensitively depends on the ratio J/U. For $U = 9$ eV, we find $p_{\rm c} = 18$ GPa for $J/U = 0.075$. In this case, the magnetization at ambient pressure is smaller than in experiment, $m = 2.05\mu_{\rm B}$, and, correspondingly, it requires less pressure to destroy the ferromagnetic bcc ground state.

Our Gutzwiller-DFT values for p_c are larger than the experimental values observed at room temperature. Our calculation applies to zero temperature while, at finite temperatures, phonon, magnon, and electronic quasiparticle contributions to the entropy also add to the difference in the Gibbs' free energies between the two phases. The latter contributions may not be unimportant because the magnetic order is destroyed at the transition. Whether the bcc or the hcp phase is stabilized by the various entropy contributions is unresolved.

We note in passing that, for simplicity, we have done the hcp calculations with the same local Hamiltonian as used for the bcc calculations, see Appendix. The latter explicitly uses cubic symmetry. Since we work in spherical approximation in any case, we do not expect that this additional approximation induces significant corrections.

In the inset of Fig. 4, we show the magnetization in bcc iron as a function of pressure when we ignore the structural transition. The magnetization changes by less than 10% from ambient pressure to $p_{\rm c}$, and it would vanish at much large pressures, $p_{\rm m} > 600$ GPa $\gg p_{\rm c}$. Therefore we find that the first-order transition at $p_{\rm c}$ is not triggered by a collapse of the magnetization in bcc iron.

3. Local occupancies

In iron, the atomic $4s$ electrons strongly hybridize with the $3d$ levels and increase their average occupancy from the atomic value $\overline{n}_d^{\rm atom} = 6$ to $\overline{n}_d^{\rm LDA} = 7.3$ in DFT(LDA). The double-counting correction used in this work, see Appendix, keeps $\overline{n}_d$ essentially constant. We find $\overline{n}_d^{\rm GDFT} = 7.2$ for $U = 9$ eV and $J/U = 0.06$. Therefore the local Coulomb interactions merely redistribute the electrons among the 1024 atomic $3d$ configurations.

The average $3d$-electron density n_d and the magnetization m do not change much as a function of (U, J). However, this does not imply that correlations are small in iron. In order to display the correlated nature of the ground state, we study some local properties.

First, we discuss the local charge distribution $n_d(n)$, which gives the probability to find n electrons in the $3d$ shell on an iron atom. Figure 5 shows $n_d(n)$ from Gutzwiller-DFT in the LDA limit, $U = 0$, and for $U = 9$ eV and $J/U = 0.05,\ 0.06$, and 0.075. For $U = 0$, we find quite a broad distribution $n_d(n)$ with significant values for $n_d(n)$ for $4 \leqslant n \leqslant 10$. For $U = 9.0$ eV and $J/U = 0.05,\ 0.06$, and 0.075, only configurations with $n = 6,\ 7$, and 8 electrons in the $3d$ shell have a substantial weight. This does not come as a surprise because the Gutzwiller correlator suppresses the occupation of local configurations that are energetically unfavorable. This behavior was also observed in previous studies [34,48].

More revealing is the local spin distribution function $n_s(s)$ shown in Fig. 6 where $n_s(s)$ gives the probability to find the local spin quantum number s on an iron atom. From $n_s(s)$, we can calculate the expectation value for the local spin as

$$\left\langle \hat{\mathbf{S}}_i^2 \right\rangle = \sum_s n_s(s) s(s+1) \equiv S_m(S_m+1). \qquad (17)$$

Here, S_m defines our average spin per atom. Figure 6 shows that the local spin distribution is fairly broad for $U = 0$. Since $n_d = 5$ is finite for $U = 0$, the local spin distribution has a finite weight even for $s = 5/2$. For $U = 9$ eV, the local configurations $3d^7$ and $3d^8$ dominate, see Fig. 5. Therefore, applying Hund's first rule, we expect to find peaks in the local spin distribution $n_s(s)$ at $s = 3/2$ and $s = 1$ which is indeed seen in Fig. 6. Concomitantly, the average spin per atom is a bit larger for $U = 9$ eV, $S_m = 1.3$ for $J/U = 0.06$, than for $U = 0, S_m^{\rm LDA} = 1.23$.

In contrast to Hund's first rule, $S_m(J)$ *decreases* as a function of the Hund's-rule coupling J. This is seen from

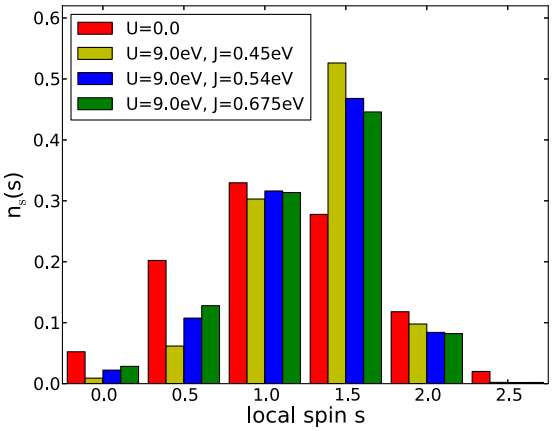

FIG. 6. Local spin distribution of iron atoms $n_s(s)$ for $U = 0$ (LDA limit) and $U = 9$ eV and $J/U = 0.05$, 0.06, and 0.075 (Gutzwiller-DFT) for optimal lattice parameters.

Fig. 6, which shows that the weight of configurations with spin $s = 0, 1/2$ increases at the expense of configurations with spin $s = 3/2$. Therefore both the overall magnetization m and the local spin S_m decrease as a function of the Hund's-rule coupling. This seems to contradict Hund's first rule which states that, in an atom, a larger J stabilizes configurations with a larger spin. Apparently, the solution to this problem must be related to the fact that we are investigating a metal in which band-magnetism dominates.

In Table I, we list the values for several quantities for $J/U = 0.05$, 0.06, and 0.075 at fixed $U = 9.0$ eV and fixed lattice parameter $a = 5.39a_B$. The data redisplay the behavior seen in Figs. 2 and 6: when we increase J/U, the magnetization m decreases. Note, however, that upon an increase of J/U, the electronic correlations actually increase, too, as can be seen from the bandwidth reduction factors (q^2). The itineracy of the electrons becomes progressively worse when the weight of local configurations is redistributed by the Gutzwiller correlator for increasing J/U. The effect of the Hund's-rule coupling on the bandwidth reduction is fairly pronounced. The (q^2) factors decrease by $\Delta(q^2) \approx 0.2$ when we vary U from zero to $U = 9.0$ eV but they change by as much as $\Delta(q^2) \approx 0.1$ for the majority spin species when we go from $J/U = 0.05$ to $J/U = 0.075$ at $U = 9$ eV. Apparently,

TABLE I. Magnetization m, bandwidth reduction factors $(q_{e_g})^2$ and $(q_{t_{2g}})^2$ for $3d(e_g)$ and $3d(t_{2g})$ electrons, respectively (resolved for majority spins and minority spins), kinetic energy $E_{\rm kin}$ per atom, and interaction energy $E_{\rm int}$ per atom; Gutzwiller-DFT data for $U = 9.0$ eV for $J/U = 0.05$, 0.06, and 0.075. The lattice parameter is fixed at $a = 5.39a_B$.

	$J/U = 0.05$	$J/U = 0.06$	$J/U = 0.075$
m/μ_B	2.49	2.24	2.05
$(q_{e_g})^2$	0.794, 0.799	0.748, 0.799	0.712, 0.795
$(q_{t_{2g}})^2$	0.790, 0.783	0.746, 0.779	0.718, 0.770
n_{e_g}	0.985, 0.350	0.985, 0.341	0.985, 0.332
$n_{t_{2g}}$	0.970, 0.546	0.925, 0.594	0.887, 0.632
$E_{\rm kin}$ (eV)	94.82	94.90	95.05
$E_{\rm int}$ (eV)	1.68	1.48	1.16

it is favorable for the kinetic energy to flip majority spins back to minority spins, i.e., there is a tendency to *reduce* the magnetization as a function of J/U. As seen from table I, the partial occupancy n_{e_g} of the e_g levels remains almost unchanged, and the reduction of the magnetization from $m = 2.49\mu_B$ at $J/U = 0.05$ to $m = 2.05\mu_B$ at $J/U = 0.075$ is generated by flipping majority-spin t_{2g} electrons.

The Hund's-rule coupling J changes the weight of isoelectronic local configurations with different spin. Apparently, this level splitting impedes the average electron transfer between atoms much more than the elimination of charge states with $n = 4$, 5, 9, and 10 by the Hubbard interaction U. The loss in kinetic energy by this "configurational hopping blockade" cannot be compensated fully by a gain in local interaction energy that is at most of the order of $\Delta E_J = (J_1 S_{m,1} - J_2 S_{m,2})$ with $\Delta E_J \approx 0.2$ eV per atom in our example. Instead, the system prefers to regain kinetic energy by reducing the magnetization at the price of loosing exchange energy; recall that in a band magnet the loss in kinetic energy is compensated by the gain in exchange energy. Since all quantities are determined self-consistently in Gutzwiller-DFT, the kinetic energy, the exchange energy, and the gain in Hund's-rule energy must be newly balanced to readjust m when we change J/U for fixed U. Apparently, in band magnets, we observe a intricate interplay between atomic and band-structure physics.

IV. BAND STRUCTURE

A. Bandwidth renormalization

We begin with a comparison of the quasiparticle bands from DFT(LDA), DFT(GGA), and Gutzwiller-DFT with $U = 9$ eV and $J/U = 0.06$ for ferromagnetic bcc iron at ambient pressure ($a = 5.39a_B$). Moreover, we compare bands from DFT(LDA) and Gutzwiller-DFT for nonmagnetic hcp iron with lattice parameter $a_{\rm hcp} = 4.60a_B$ and $(c/a)_{\rm hcp} = 1.60$; the results change marginally when we use the ideal ratio $(c/a)_{\rm ideal} = \sqrt{8/3} = 1.63$.

In order to obtain smooth band plots and to include the effects of the spin-orbit coupling on the band structure perturbatively, see Sec. IV B 1, we introduced a further post-processing step. The Gutzwiller-Kohn-Sham quasiparticles were used to generate maximally-localized Wannier functions using WANNIER90 [56], from which we constructed a tight-binding model to calculate the band structure at arbitrary $\mathbf{k}$ points. These Wannier functions are used only for plotting purposes, and are unrelated to those chosen to perform the self-consistent calculations.

We checked that the tight-binding dispersion relation agrees with the calculated energy levels from QUANTUM ESPRESSPO for our selected independent $\mathbf{k}$ points in the Brillouin zone. The small wiggles in the $4s$ bands close to the Γ point seen in Fig. 7 are a result of the tight-binding fit. We disregard the problem because this does not influence the $3d$ bands close to the Fermi energy and has no effect on the total energy, which is calculated using the original quasiparticles.

1. *Ferromagnetic bcc iron*

In Fig. 7, we compare the band structure for ferromagnetic bcc iron from DFT(LDA) and from Gutzwiller-DFT

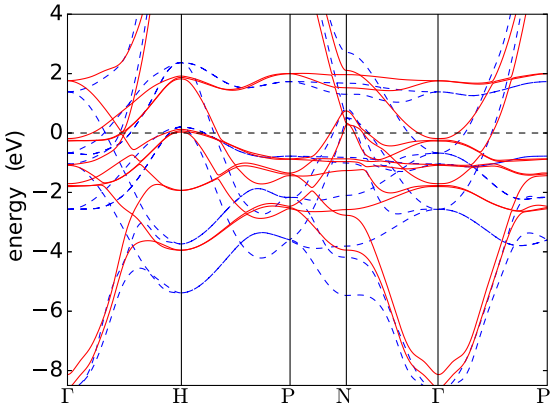

FIG. 7. Comparison between DFT(LDA) bands (blue, dashed lines) for $a^{\mathrm{LDA}} = 5.21a_{\mathrm{B}}$ and bands from Gutzwiller-DFT (red, full lines) for the optimal atomic parameters $U = 9.0$ eV, $J = 0.54$ eV, and $a = 5.39a_{\mathrm{B}}$ for ferromagnetic bcc iron. For clarity, we do not discriminate between majority and minority spin bands. The Fermi energy is at $E_{\mathrm{F}} = 0$ (dashed black horizontal line).

for $U = 9.0$ eV and $J = 0.54$ eV. Both calculations are performed at the optimal lattice parameter, $a^{\mathrm{LDA}} = 5.21a_{\mathrm{B}}$ and $a^{\mathrm{GDFT}} = 5.39a_{\mathrm{B}}$. Figure 7 shows the common characteristics of correlation-induced effects on energy bands. First, the uncorrelated, $4sp$-type parts of the quasiparticle bands deep below the Fermi energy do not differ much, e.g., the lowest $4sp$-type majority bands are at $\Gamma^{\mathrm{LDA}}_{\mathrm{low},\uparrow} = 9.0$ eV and $\Gamma^{\mathrm{G\text{-}DFT}}_{\mathrm{low},\uparrow} = 8.57$ eV below the Fermi energy $E_{\mathrm{F}} = 0$. Minor deviations are related to slightly different lattice parameters and $3d$-electron numbers $\overline{n}_d$ in DFT(LDA) and Gutzwiller-DFT.

Second, the Gutzwiller-correlated $3d$-type parts of the quasiparticle bands close to the Fermi energy are shifted with respect to the DFT(LDA) bands, and the bandwidths of the correlated bands are reduced by factors proportional to $(q_{t_{2g}})^2$ and $(q_{e_g})^2$ for the $3d$-t_{2g} and $3d$-e_g majority and minority bands. Note that, due to the hybridization of the quasiparticles, a meaningful symmetry character can only be assigned to the bands at high-symmetry points in the Brillouin zone.

The bandwidth reduction in iron is not as strong as in nickel. Nevertheless, for selected symmetry points, the discrepancies between the quasiparticle bands from DFT(LDA) and Gutzwiller-DFT are quite large. For example, at the H point in the Brillouin zone, we find a bandwidth reduction for the majority band by 36%, from $H^{\mathrm{LDA}}_{\mathrm{low},\uparrow} = 5.38$ eV down to $H^{\mathrm{G\text{-}DFT}}_{\mathrm{low},\uparrow} = 3.94$ eV, in good agreement with experiment, $H_{\mathrm{low},\uparrow} = 3.8$ eV [57]. Likewise, at the N point in the Brillouin zone there is a majority spin band at $N_{\mathrm{low},\uparrow} = 4.5$ eV below the Fermi energy in experiment [57], in comparison with $N^{\mathrm{LDA}}_{\mathrm{low},\uparrow} = 5.47$ eV in DFT(LDA) and $N^{\mathrm{G\text{-}DFT}}_{\mathrm{low},\uparrow} = 3.90$ eV in Gutzwiller-DFT. At the Γ point, the bandwidth reduction is only about 10% for bands close to the Fermi edge. In addition, the bandwidth renormalization at the Γ point is overlaid with a bandshift of about 0.4 eV.

For completeness, we show the band structure for ferromagnetic bcc iron from Gutzwiller-DFT for $U = 9.0$ eV and $J = 0.54$ eV in comparison with those from (scalar relativistic) DFT(GGA) calculations in Fig. 8. The two band structures differ less than in Fig. 7 because our DFT(GGA)

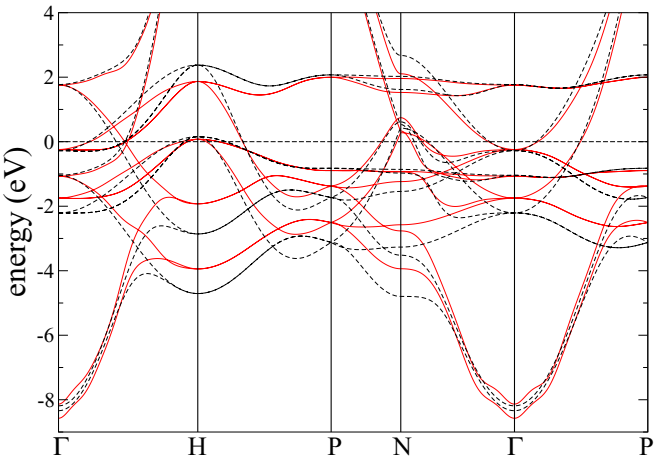

FIG. 8. Comparison between DFT(GGA) bands (black, dashed lines) for $a_{\mathrm{GGA}} = 5.39a_{\mathrm{B}}$ and bands from Gutzwiller-DFT (red, full lines) for the optimal atomic parameters $U = 9.0$ eV, $J = 0.54$ eV, and $a = 5.39a_{\mathrm{B}}$ for ferromagnetic bcc iron. For clarity, we do not discriminate between majority and minority spin bands. The Fermi energy is at $E_{\mathrm{F}} = 0$ (dashed horizontal line).

provides the same equilibrium lattice parameter as used in Gutzwiller-DFT, $a_{\mathrm{GGA}} = 5.39a_{\mathrm{B}}$. The bandwidth of the $3d$ electrons from the DFT(LDA) is calculated for $a_{\mathrm{LDA}} = 5.21a_{\mathrm{B}}$ so that the $3d$ orbitals have a larger overlap in DFT(LDA) than in DFT(GGA), and the $3d$ bandwidth is larger in LDA than in GGA. Nevertheless, the correlations in the Gutzwiller approach lead to an additional bandwidth reduction of the d bands across the Brillouin zone.

2. *Nonmagnetic hcp iron*

In Fig. 9, we compare the band structure for nonmagnetic hcp iron from DFT(LDA) and from Gutzwiller-DFT for $U = 9.0$ eV and $J = 0.54$ eV. Both calculations are performed at

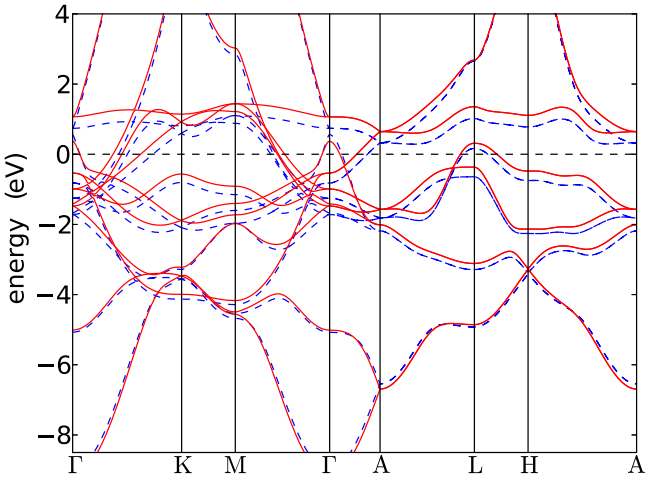

FIG. 9. Comparison between DFT(LDA) bands (blue, dashed lines) and bands from Gutzwiller-DFT (red, full lines) for the atomic parameters $U = 9.0$ eV and $J = 0.54$ eV for paramagnetic hcp iron at $a = 4.60a_{\mathrm{B}}$ and $c/a = 1.60$. The Fermi energy is at $E_{\mathrm{F}} = 0$ (dashed black horizontal line).

the lattice parameter $a = 4.60a_B$ and $c/a = 1.60$ so that the unit-cell volume is $v_0 = \sqrt{3}/2(a^2/2)c = 67.4a_B^3$. The partial densities are almost identical, $\overline{n}_d = 7.3$.

As for ferromagnetic bcc iron, the uncorrelated, $4sp$-type parts of the quasiparticle bands deep below or high above the Fermi energy do not differ much. Again, the Gutzwiller-correlated $3d$-type parts of the quasiparticle bands close to the Fermi energy are shifted with respect to the DFT(LDA) bands, and the bandwidths of the correlated bands are reduced. The Fermi-liquid properties (Fermi surface topology, wave vectors, velocities) differ only quantitatively.

B. Comparison with ARPES measurements

1. Inclusion of spin-orbit coupling

As the effective parameter for the spin-orbit interaction we choose $\zeta = 0.06$ eV, in agreement with previous studies [58,59]. The small value permits a perturbative treatment of the spin-orbit coupling. In effect, it leads to negligibly small changes in the band structures but for avoided crossings of majority and minority bands where it induces band gaps of the order of ζ. Since some of the avoided crossings are energetically close to the Fermi energy, the spin-orbit interaction has some noticeable effect on the positions of the Fermi points and the Fermi velocities.

For our perturbative treatment, we start from the majority and minority bands as calculated from Gutzwiller-DFT for ($U = 9.0$ eV and $J = 0.54$ eV) at $a = 5.39a_B$ and use the program WANNIER90 [56] to derive a tight-binding Hamilton operator. Then, the two block-diagonal parts of the Hamiltonian for the majority and minority bands are coupled by the spin-orbit interaction. We obtain the band structure with spin-orbit coupling from the diagonalization of this effective Hamilton matrix. For larger values of ζ, a fully self-consistent treatment of the spin-orbit interaction is necessary that requires the formulation of a relativistic Gutzwiller-DFT.

2. Quasiparticle bands close to the Fermi energy

Figures 10 to 13 show an overlay of ARPES data from Schäfer *et al.* [35] with the results of our perturbative spin-orbit calculation based on the Gutzwiller-DFT. A quantitative comparison between theory and experiment is given in Table II where we list the Fermi wave numbers and velocities for various directions and Fermi sheets for LDA+Gutzwiller and ARPES [35]. For completeness, we also include in the table values from our fully relativistic GGA calculations, see Sec. II C for details.

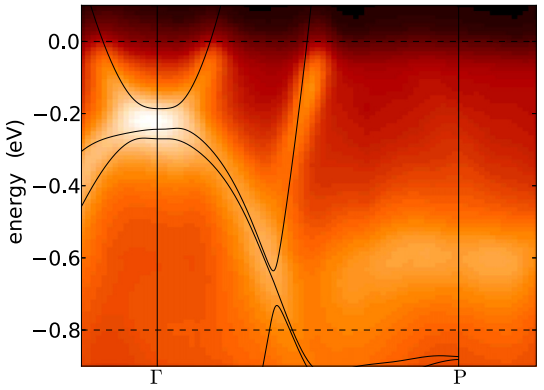

FIG. 10. Overlay of quasiparticle bands from LDA+Gutzwiller for $U = 9.0$ eV, $J = 0.54$ eV, and lattice parameter $a = 5.39a_B$ with ARPES data along the Γ-P direction [35].

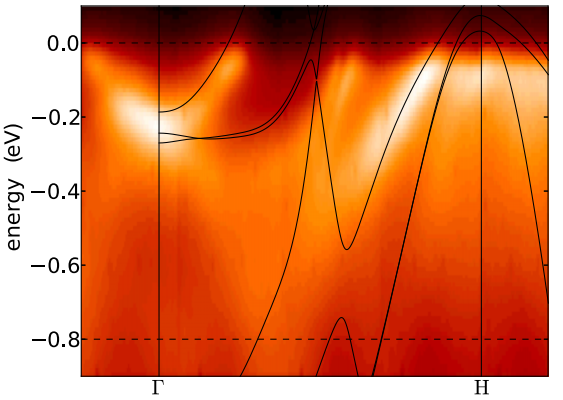

FIG. 11. Overlay of quasiparticle bands from LDA+Gutzwiller for $U = 9.0$ eV, $J = 0.54$ eV, and lattice parameter $a = 5.39a_B$ with ARPES data along the Γ-H direction [35].

We begin our discussion with the Γ-P high-symmetry line in the Brillouin zone. From Fig. 10 we see that, close to the Γ point, we observe a very good agreement between LDA+Gutzwiller and experimental data for the Fermi sheet VI. Moreover, the Fermi wave numbers and the velocities agree very well, as seen from Table II. Our LDA+Gutzwiller improves the theoretical values for the Fermi velocity. The mass ratio between theory and experiment reduces from $v_d/v_R = 1.9$ in DFT(GGA) to $v_G/v_R = 1.6$ in LDA+Gutzwiller. Note that the mass ratio is unity for a perfect agreement between theory and experiment, and it is larger than unity when the theoretical mass is smaller than measured value, $v/v_R = m_R/m$.

The largest discrepancies between experiment and LDA+Gutzwiller theory are seen at and around the P point. The LDA+Gutzwiller bands are about 0.3 eV below the ARPES bands, and the discrepancy in LDA+Gutzwiller is actually *worse* than in LDA(GGA). We do not have an explanation for this deviation.

Half way on the line Γ-P there is the Fermi sheet I. For this band, the values for the Fermi wavenumbers from DFT(GGA) and LDA+Gutzwiller are very close to the experimental value but the Fermi velocities deviate considerably, even though LDA+Gutzwiller has a slightly better mass ratio, $v_G/v_R = 2.8$ versus $v_d/v_R = 3.4$.

In Fig. 11, we plot the data overlay along the high-symmetry line Γ-H. As discussed before, the agreement of the quasiparticle bands, wave numbers, and velocities of Fermi sheet VI close to the Γ point is very good. The same holds true for the Fermi sheet II close to the H point.

For the majority Fermi sheet I half way between the points Γ and H we find a large mass ratio as in LDA(GGA), $v_G/v_R = 3.0$ versus $v_d/v_R = 2.1$. Note, however, that several bands meet at the Fermi energy with the same Fermi wave number, and the spin-orbit coupling leads to a splitting of

TABLE II. Comparison of Fermi wave numbers and velocities for various Fermi sheets between fully relativistic DFT(GGA), LDA+Gutzwiller for $U = 9.0$ eV, $J = 0.54$ eV, and $a = 5.39a_B$, and ARPES results [35]. FS stands for the Fermi sheet, k_F is the Fermi wave number, and $v_F = v/\hbar = \hbar k_F/m$ is the Fermi velocity.

Direction	Spin	FS	k_F GGA ($Å^{-1}$)	k_F LDA+G ($Å^{-1}$)	k_F ARPES ($Å^{-1}$)	Slope v_d GGA (eVÅ)	Slope v_G LDA+G (eVÅ)	Slope v_R ARPES (eVÅ)	Mass ratio v_d/v_R	Mass ratio v_G/v_R
Γ-*P*	Min.	VI	0.31	0.33	0.32	1.66	1.38	0.88	1.9	1.6
	Maj.	I	0.95	0.94	0.97	4.74	3.86	1.40	3.4	2.8
Γ-*H*	Min.	VI	0.47	0.49	0.46	1.08	0.83	0.72	1.5	1.2
	Maj.	I	1.09	1.10	1.08	2.36	3.35	1.12	2.1	3.0
		II	1.94	1.93	1.70	0.64	0.58	0.67	1.0	0.9
Γ-*N*	Min.	VI	0.33	0.35	0.36	1.52	1.25	0.80	1.9	1.6
	Maj.	I	1.21	1.21	1.22	1.89	1.53	1.16	1.6	1.3
H-*P*	Min.	V	0.65	0.64	0.68	4.82	4.16	1.79	2.7	2.3

bands. Therefore it is difficult to determine the Fermi velocity due to the sequence of crossings. This region around the Fermi energy is not very suitable for a meaningful comparison between theory and experiment.

In Fig. 12, we plot the data overlay along the high-symmetry line N-Γ. In experiment, the intensity along this direction is suppressed close to the point N due to matrix-element effects. However, we reproduce a crossing of the Fermi energy close to the N point and the slope of the bands agree quite well.

For the minority band VI close to the Γ point, we find a mass ratio of $v_G/v_R = 1.6$, versus $v_d/v_R = 1.9$ in DFT(GGA). For the majority band I half way between Γ and N, we find a mass ratio of $v_G/v_R = 1.3$, versus $v_d/v_R = 1.6$ in DFT(GGA). In both cases, we find a slight improvement over the DFT(GGA) results. Half way between the points N and Γ, it seems as if the LDA+Gutzwiller bands at energies of about -0.5 eV do not agree very well with the ARPES bands but better experimental data are needed for a definitive statement.

Lastly, we take a look at the direction H-P in Fig. 13. As already seen from the other plots, the agreement at and around the point H is quite good, while the comparison at point P reveals some discrepancies between theory and experiment. In addition, the ARPES data show some distinct Fermi level crossing half way between H and P. The LDA+Gutzwiller approach yields a Fermi wave number for this crossing that deviates slightly from experiment with a mass ratio $v_G/v_R = 2.3$ versus $v_d/v_R = 2.7$ in DFT(GGA).

Depending on the Fermi wave vector, the quasiparticle mass in Gutzwiller-DFT is some 20% larger than in DFT(GGA). A similar mass enhancement is observed in DFT(DMFT) calculations [18,51]. However, as seen from Table II, the mass ratio between theory and experiment is consistently larger than unity, $v_G/v_R = m_R/m_G > 1$, and strongly depends on the Fermi wave vector. The correlation-induced mass enhancement alone cannot account for the large mass renormalization as seen in experiment. The resolution of this discrepancy remains one of the incompletely understood problems for iron and other magnetic materials.

V. CONCLUSIONS

In this work, we used the Gutzwiller-DFT for a detailed study of the ground-state properties and the quasiparticle band structure of iron. We find that, for a Hubbard interaction of $U = 9$ eV and a Hund's-rule coupling of $J = 0.54$ eV, we reproduce the experimental lattice parameter and magnetization, and we obtain the bulk modulus of ferromagnetic bcc iron in very good agreement with experiment. Upon increasing pressure we qualitatively reproduce the transition to nonmagnetic hcp iron.

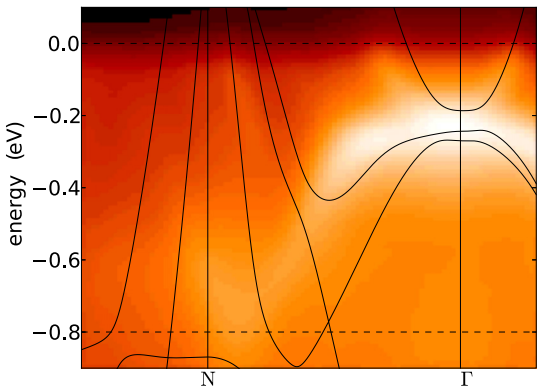

FIG. 12. Overlay of quasiparticle bands from LDA+Gutzwiller for $U = 9.0$ eV, $J = 0.54$ eV, and lattice parameter $a = 5.39a_B$ with ARPES data along the N-Γ direction [35].

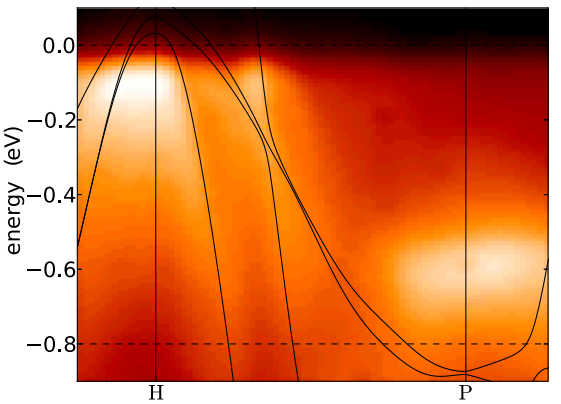

FIG. 13. Overlay of quasiparticle bands from LDA+Gutzwiller for $U = 9.0$ eV, $J = 0.54$ eV, and lattice parameter $a = 5.39a_B$ with ARPES data along the H-P direction [35].

We find that the ground-state magnetization sensitively depends on the Hund's-rule coupling J. In contrast to physical intuition, an increase of J leads to a decrease of the magnetization. For example, at $U = 9$ eV, an increase from $J = 0.45$ eV to $J = 0.68$ eV decreases the magnetization from $m = 2.5\mu_B$ to $m = 2.05\mu_B$. The Hund's-rule coupling generates a splitting of isoelectronic atomic levels, and the corresponding redistribution of local occupancies considerably impedes the electrons' motion through the lattice ("configurational hopping blockade"). In a band magnet, the delicate balance between the Hund's-rule and exchange-energy gains against the corresponding losses in kinetic energy makes the magnetization sensitive to the Hund's-rule coupling. Therefore the absolute value of J is much more decisive for physical quantities than the value of the Hubbard interaction. For the calculation of some physical quantities, a larger value of J can be "traded in" for a smaller U.

Gutzwiller-DFT renormalizes the quasiparticle bands as obtained from DFT(LDA). While the $4sp$-type parts are almost unchanged, the $3d$ bands are shifted and their width is reduced, in agreement with experiment. Shifts and renormalizations are also observed when we compare the Gutzwiller-DFT results with GGA calculations although the effects are quantitatively smaller. The applied double-counting corrections make sure that the average $3d$-electron density remains essentially the same, $\bar{n}_d \approx 7.2$. The agreement between the Gutzwiller quasiparticle bands with ARPES data is fairly good when we take spin-orbit effects into account perturbatively. In general, Gutzwiller-DFT agrees better with ARPES data than DFT, both in the LDA and GGA approximations.

Finally, we note that the optimal atomic parameters in the present Gutzwiller-DFT study on iron resemble those used by Deng *et al.* [20,21] but are sensibly higher than those used in a more recent Gutzwiller-DFT work by Borghi *et al.* [33] who propound a U-parameter of $U_B = 2.5$ eV for iron that is significantly smaller than our values. Part of the discrepancy is probably due to their different choice of energy window and basis set for the construction of the many-body model. However, there are also substantial differences already at the bare DFT(LDA) level ($U = J = 0$); Borghi *et al.* use a localized orbital code (SIESTA) whose results deviate from other DFT codes for iron. Table III of Ref. [33] gives the lattice constant $a_{\text{Borghi}} = 2.83$ Å $= 5.35a_B$, while we find $a_0 = 5.2a_B$, in agreement with earlier LDA-LAPW calculations [1]. Since the lattice constant monotonically increases as a function of U, see Fig. 1, it is not surprising that Borghi *et al.* require a smaller Hubbard interaction to reproduce the experimental lattice parameter $a = 5.42a_B$, and claim a different role of electronic correlations in iron.

Despite the improvements of Gutzwiller-DFT and DFT(DMFT) over standard DFT(LDA and GGA), the theoretical Fermi velocities are typically too large, i.e., the quasiparticle masses from theory are too low in comparison with experiment. This systematic discrepancy could have several reasons. First, it might be necessary to process the theoretical band structures further to mimic the excitation process in ARPES experiments [60]. However, this approach could not explain why the systematic mass enhancement is also seen in de Haas-van Alphen measurements for iron and ferromagnetic nickel compounds [61]. Therefore it is more likely that the effective mass results from the interaction of the quasiparticles with low-energy magnetic excitations, i.e., magnetic polarons exist near the Fermi energy [62]. At present, however, the inclusion of long wave-length excitations is beyond the Gutzwiller-DFT.

ACKNOWLEDGMENTS

We thank R. Claessen for helpful discussions on the mass enhancement in iron, and him and J. Schäfer for sending us the figures of their experimental data. L.B. would like to thank M. Aichhorn for useful discussion and for pointing out reference [18]. The work was supported in part by the SPP 1458 of the Deutsche Forschungsgemeinschaft (BO 3536/2 and GE 746/10). The figures in this publication were created using the matplotlib library [63].

APPENDIX: ATOMIC INTERACTIONS AND DOUBLE COUNTING

For the $3d$ shell of e_g and t_{2g} orbitals in transition metals, the local Hamiltonian (2) reads ($\sigma = \uparrow, \downarrow$)

$$\begin{aligned}\hat{V}_{\text{loc}} = &\frac{1}{2}\sum_{c,\sigma} U(c,c)\hat{n}_{c,\sigma}\hat{n}_{c',\bar{\sigma}} + \frac{1}{2}\sum_{\substack{c(\neq)c'\\ \sigma,\sigma'}} \widetilde{U}_{\sigma,\sigma'}(c,c')\hat{n}_{c,\sigma}\hat{n}_{c',\sigma'}\\ &+\frac{1}{2}\sum_{c(\neq)c'} J(c,c')(\hat{c}^\dagger_{c,\uparrow}\hat{c}^\dagger_{c,\downarrow}\hat{c}_{c',\downarrow}\hat{c}_{c',\uparrow} + \text{H.c.})\\ &+\frac{1}{2}\sum_{c(\neq)c';\sigma} J(c,c')\hat{c}^\dagger_{c,\sigma}\hat{c}^\dagger_{c',\bar{\sigma}}\hat{c}_{c,\bar{\sigma}}\hat{c}_{c',\sigma}\\ &+\Bigg[\sum_{t;\sigma,\sigma'}(T(t) - \delta_{\sigma,\sigma'}A(t))\hat{n}_{t,\sigma}\hat{c}^\dagger_{u,\sigma'}\hat{c}_{v,\sigma'}\\ &+\sum_{t,\sigma} A(t)(\hat{c}^\dagger_{t,\sigma}\hat{c}^\dagger_{t,\bar{\sigma}}\hat{c}_{u,\bar{\sigma}}\hat{c}_{v,\sigma} + \hat{c}^\dagger_{t,\sigma}\hat{c}^\dagger_{u,\bar{\sigma}}\hat{c}_{t,\bar{\sigma}}\hat{c}_{v,\sigma})\\ &+\sum_{\substack{t(\neq)t'(\neq)t''\\ e,\sigma,\sigma'}} S(t,t';t'',e)\hat{c}^\dagger_{t,\sigma}\hat{c}^\dagger_{t',\sigma'}\hat{c}_{t'',\sigma'}\hat{c}_{e,\sigma} + \text{H.c.}\Bigg].\end{aligned} \tag{A1}$$

Note that the factors $1/2$ in the first three lines have been erroneously missing in our previous publications [8] and [48]. Here, $\widetilde{U}_{\sigma,\sigma'}(c,c') = U(c,c') - \delta_{\sigma,\sigma'}J(c,c')$, and we suppressed the site index $\mathbf{R}$. The index c sums over all five d orbitals, while t and e are indices for the three t_{2g} orbitals with symmetries xy, xz, and yz and the two e_g orbitals with symmetries $u = 3z^2 - r^2$ and $v = x^2 - y^2$, respectively. Of all the parameters $U(c,c'), J(c,c'), A(t), T(t), S(t,t';t'',e)$ only ten are independent in cubic symmetry [8,64]. When we assume that all $3d$ orbitals have the same radial wave function ("spherical approximation"), all parameters are determined by, e.g., the three Racah parameters A, B, C. They are related to the Slater-Condon parameters via

$$A = F^{(0)} - \frac{F^{(4)}}{9}, \quad B = \frac{1}{49}\left(F^{(2)} - \frac{5}{9}F^{(4)}\right),$$
$$C = \frac{5}{63}F^{(4)}, \tag{A2}$$

or, inversely,

$$F^{(0)} = A + \frac{7}{5}C \quad , \quad F^{(2)} = 49B + 7C \quad , \quad F^{(4)} = \frac{63}{5}C. \tag{A3}$$

Explicit expressions for the relations between the parameters in Eq. (A1) and the Racah parameters A, B, and C can be found in Appendix C of Ref. [8]. For comparison with other work, we introduce the Coulomb interaction between electrons in the same $3d$ orbitals (intraorbital Hubbard interaction),

$$U = A + 4B + 3C, \tag{A4}$$

the average Coulomb interaction between electrons in different orbitals (interorbital Hubbard interaction),

$$U' = \frac{1}{10}\sum_{c<c'} U(c,c') = A - B + C, \tag{A5}$$

and the average Hund's-rule exchange interaction,

$$J = \frac{1}{10}\sum_{c<c'} J(c,c') = \frac{5}{2}B + C. \tag{A6}$$

These three quantities are not independent but related by the symmetry relation $U' = U - 2J$. This means that by choosing two of these parameters (e.g., U and J) the three Racah parameters, and therefore all the parameters in Eq. (A1) are not uniquely defined. Hence we use the additional relation $C/B = 4$, which is a reasonable assumption for transition metals [64]. It corresponds to $F^{(2)}/F^{(4)} = 55/36 = 1.53$, in agreement with the estimate $F^{(2)}/F^{(4)} \approx 1.60 = 8/5$ by de Groot *et al.* [50]. For completeness, we give the dependencies of the Racah parameters on U and J

$$A = U - \frac{32}{13}J, \quad B = \frac{2}{13}J, \quad C = \frac{8}{13}J. \tag{A7}$$

In our previous study on nickel [8], we have tested three different types of double-counting corrections that had been proposed in the literature. It turned out that only one of them leads to sensible results for nickel. As for nickel [8], we employ the widely used functional [37,38]

$$V_{\mathrm{dc}} = \frac{\bar{U}}{2}\bar{n}(\bar{n}-1) - \frac{\bar{J}}{2}\sum_{\sigma}\bar{n}_\sigma(1-\bar{n}_\sigma). \tag{A8}$$

For $3d$ electrons, we have

$$F^{(0)} = \bar{U} = \tfrac{1}{5}(U + 4U') \quad , \quad \bar{J} = \bar{U} - U' + J, \tag{A9}$$

and

$$\bar{n}_\sigma \equiv \sum_{c=1}^{N_c} C^{\mathrm{G}}_{c,c;\sigma}, \quad \bar{n} \equiv \bar{n}_\uparrow + \bar{n}_\downarrow, \tag{A10}$$

where N_c is the number of correlated orbitals, in our case, $N_c = 5$. Moreover,

$$C^{\mathrm{G}}_{c,c;\sigma} = \frac{\langle\Psi_{\mathrm{G}}|\hat{c}^{+}_{\mathbf{R},c,\sigma}\hat{c}_{\mathbf{R},c,\sigma}|\Psi_{\mathrm{G}}\rangle}{\langle\Psi_{\mathrm{G}}|\Psi_{\mathrm{G}}\rangle} = \langle\psi_0|\hat{c}^{+}_{\mathbf{R},c,\sigma}\hat{c}_{\mathbf{R},c,\sigma}|\psi_0\rangle \tag{A11}$$

is the σ-electron density for the correlated $3d$ orbital c in the Gutzwiller wave function. Note that the second equality only holds in the limit of infinite dimensions for our e_g-t_{2g} orbital structure [8].

[1] C. S. Wang, B. M. Klein, and H. Krakauer, Phys. Rev. Lett. **54**, 1852 (1985).
[2] S. K. Bose, O. V. Dolgov, J. Kortus, O. Jepsen, and O. K. Andersen, Phys. Rev. B **67**, 214518 (2003).
[3] L. Stixrude, R. E. Cohen, and D. J. Singh, Phys. Rev. B **50**, 6442 (1994).
[4] M. Ekman, B. Sadigh, K. Einarsdotter, and P. Blaha, Phys. Rev. B **58**, 5296 (1998).
[5] J. P. Perdew, K. Burke, and M. Ernzerhof, Phys. Rev. Lett. **77**, 3865 (1996).
[6] G. Steinle-Neumann, L. Stixrude, and R. E. Cohen, Phys. Rev. B **60**, 791 (1999).
[7] G. Y. Guo and H. H. Wang, Chin. J. Phys. **38**, 949 (2000).
[8] T. Schickling, J. Bünemann, F. Gebhard, and W. Weber, New J. Phys. **16**, 93034 (2014).
[9] K. Glazyrin, L. V. Pourovskii, L. Dubrovinsky, O. Narygina, C. McCammon, B. Hewener, V. Schünemann, J. Wolny, K. Muffler, A. I. Chumakov, W. Crichton, M. Hanfland, V. B. Prakapenka, F. Tasnádi, M. Ekholm, M. Aichhorn, V. Vildosola, A. V. Ruban, M. I. Katsnelson, and I. A. Abrikosov, Phys. Rev. Lett. **110**, 117206 (2013).
[10] J. Hubbard, Proc. Royal Soc. A **276**, 238 (1963)
[11] M. C. Gutzwiller, Phys. Rev. Lett. **10**, 159 (1963).
[12] J. Hubbard, Proc. Royal Soc. A **277**, 237 (1964)
[13] M. C. Gutzwiller, Phys. Rev. **134**, A923 (1964).
[14] G. Kotliar, S. Y. Savrasov, K. Haule, V. S. Oudovenko, O. Parcollet, and C. A. Marianetti, Rev. Mod. Phys. **78**, 865 (2006).
[15] D. Vollhardt, Ann. Phys. **524**, 1 (2012).
[16] E. Gull, A. J. Millis, A. I. Lichtenstein, A. N. Rubtsov, M. Troyer, and P. Werner, Rev. Mod. Phys. **83**, 349 (2011).
[17] A. S. Belozerov and V. I. Anisimov, J. Phys. Condens. Matter **26**, 375601 (2014).
[18] L. V. Pourovskii, J. Mravlje, M. Ferrero, O. Parcollet, and I. A. Abrikosov, Phys. Rev. B **90**, 155120 (2014).
[19] K. M. Ho, J. Schmalian, and C. Z. Wang, Phys. Rev. B **77**, 073101 (2008).
[20] X. Deng, X. Dai, and Z. Fang, Europhys. Lett. **83**, 37008 (2008).
[21] X. Y. Deng, L. Wang, X. Dai, and Z. Fang, Phys. Rev. B **79**, 075114 (2009).
[22] G.-T. Wang, X. Dai, and Z. Fang, Phys. Rev. Lett. **101**, 066403 (2008).
[23] G. T. Wang, Y. Qian, G. Xu, X. Dai, and Z. Fang, Phys. Rev. Lett. **104**, 047002 (2010).
[24] H. Weng, G. Xu, H. Zhang, S.-C. Zhang, X. Dai, and Z. Fang, Phys. Rev. B **84**, 060408 (2011).
[25] Y. X. Yao, J. Schmalian, C. Z. Wang, K. M. Ho, and G. Kotliar, Phys. Rev. B **84**, 245112 (2011).
[26] M.-F. Tian, X. Deng, Z. Fang, and X. Dai, Phys. Rev. B **84**, 205124 (2011).

[27] N. Lanatà, H. U. R. Strand, X. Dai, and B. Hellsing, Phys. Rev. B **85**, 035133 (2012).

[28] N. Lanatà, H. U. R. Strand, G. Giovannetti, B. Hellsing, L. de' Medici, and M. Capone, Phys. Rev. B **87**, 045122 (2013).

[29] N. Lanatà, Y.-X. Yao, C.-Z. Wang, K.-M. Ho, J. Schmalian, K. Haule, and G. Kotliar, Phys. Rev. Lett. **111**, 196801 (2013).

[30] N. Lanatà, Y.-X. Yao, C.-Z. Wang, K.-M. Ho, and G. Kotliar, Phys. Rev. B **90**, 161104 (2014).

[31] R. Dong, X. Wan, X. Dai, and S. Y. Savrasov, Phys. Rev. B **89**, 165122 (2014).

[32] N. Lanatà, Y. Yao, C.-Z. Wang, K.-M. Ho, and G. Kotliar, Phys. Rev. X **5**, 011008 (2015).

[33] G. Borghi, M. Fabrizio, and E. Tosatti, Phys. Rev. B **90**, 125102 (2014).

[34] T. Schickling, F. Gebhard, J. Bünemann, L. Boeri, O. K. Andersen, and W. Weber, Phys. Rev. Lett. **108**, 036406 (2012).

[35] J. Schäfer, M. Hoinkis, E. Rotenberg, P. Blaha, and R. Claessen, Phys. Rev. B **72**, 155115 (2005).

[36] J. Bünemann, F. Gebhard, T. Schickling, and W. Weber, Phys. Status Solidi (b) **249**, 1282 (2012).

[37] V. I. Anisimov, J. Zaanen, and O. K. Andersen, Phys. Rev. B **44**, 943 (1991).

[38] A. I. Liechtenstein, V. I. Anisimov, and J. Zaanen, Phys. Rev. B **52**, R5467 (1995).

[39] P. Giannozzi, S. Baroni, N. Bonini, M. Calandra, R. Car, C. Cavazzoni, D. Ceresoli, G. L. Chiarotti, M. Cococcioni, I. Dabo, A. D. Corso, S. de Gironcoli, S. Fabris, G. Fratesi, R. Gebauer, U. Gerstmann, C. Gougoussis, A. Kokalj, M. Lazzeri, L. Martin-Samos, N. Marzari, F. Mauri, R. Mazzarello, S. Paolini, A. Pasquarello, L. Paulatto, C. Sbraccia, S. Scandolo, G. Sclauzero, A. P. Seitsonen, A. Smogunov, P. Umari, and R. M. Wentzcovitch, J. Phys. Condens. Matter **21**, 395502 (2009).

[40] See Supplemental Material at http://link.aps.org/supplemental/10.1103/PhysRevB.93.205151 for the implementation of the Gutzwiller-DFT in QUANTUM ESPRESSO.

[41] H. L. Zhang, S. Lu, M. P. J. Punkkinen, Q.-M. Hu, B. Johansson, and L. Vitos, Phys. Rev. B **82**, 132409 (2010).

[42] H. Danan, A. Herr, and A. J. P. Meyer, J. Appl. Phys. **39**, 669 (1968).

[43] A. A. Katanin, A. I. Poteryaev, A. V. Efremov, A. O. Shorikov, S. L. Skornyakov, M. A. Korotin, and V. I. Anisimov, Phys. Rev. B **81**, 045117 (2010).

[44] I. Leonov, A. I. Poteryaev, V. I. Anisimov, and D. Vollhardt, Phys. Rev. Lett. **106**, 106405 (2011).

[45] I. Leonov, A. I. Poteryaev, Y. N. Gornostyrev, A. I. Lichtenstein, M. I. Katsnelson, V. I. Anisimov, and D. Vollhardt, Sci. Rep. **4**, 5585 (2014)

[46] A. I. Lichtenstein, M. I. Katsnelson, and G. Kotliar, Phys. Rev. Lett. **87**, 067205 (2001).

[47] T. Miyake, F. Aryasetiawan, and M. Imada, Phys. Rev. B **80**, 155134 (2009).

[48] T. Schickling, F. Gebhard, and J. Bünemann, Phys. Rev. Lett. **106**, 146402 (2011).

[49] F. Aryasetiawan, K. Karlsson, O. Jepsen, and U. Schönberger, Phys. Rev. B **74**, 125106 (2006).

[50] F. M. F. de Groot, J. C. Fuggle, B. T. Thole, and G. A. Sawatzky, Phys. Rev. B **42**, 5459 (1990).

[51] J. Sánchez-Barriga, J. Fink, V. Boni, I. Di Marco, J. Braun, J. Minár, A. Varykhalov, O. Rader, V. Bellini, F. Manghi, H. Ebert, M. I. Katsnelson, A. I. Lichtenstein, O. Eriksson, W. Eberhardt, and H. A. Dürr, Phys. Rev. Lett. **103**, 267203 (2009).

[52] A. P. Jephcoat, H. K. Mao, and P. M. Bell, J. Geophys. Res.: Solid Earth **91**, 4677 (1986).

[53] O. K. Andersen, J. Madsen, U. K. Poulsen, O. Jepsen, and J. Kollar, Physica B **86–88**, 249 (1977).

[54] D. Bancroft, E. L. Peterson, and S. Minshall, J. Appl. Phys. **27**, 291 (1956).

[55] V. Iota, J.-H. P. Klepeis, C.-S. Yoo, J. Lang, D. Hasekl, and G. Srajer, Appl. Phys. Lett. **90**, 042505 (2007).

[56] A. A. Mostofi, J. R. Yates, Y.-S. Lee, I. Souza, D. Vanderbilt, and N. Marzari, Comput. Phys. Commun. **178**, 685 (2008).

[57] A. M. Turner, A. W. Donoho, and J. L. Erskine, Phys. Rev. B **29**, 2986 (1984).

[58] M. Singh, C. S. Wang, and J. Callaway, Phys. Rev. B **11**, 287 (1975)

[59] Y. Yao, L. Kleinman, A. H. MacDonald, J. Sinova, T. Jungwirth, D.-S. Wang, E. Wang, and Q. Niu, Phys. Rev. Lett. **92**, 037204 (2004).

[60] A. L. Walter, J. D. Riley, and O. Rader, New J. Phys. **12**, 013007 (2010).

[61] G. G. Lonzarich, J. Magn. Magn. Mater. **45**, 43 (1984).

[62] J. Schäfer, D. Schrupp, E. Rotenberg, K. Rossnagel, H. Koh, P. Blaha, and R. Claessen, Phys. Rev. Lett. **92**, 097205 (2004).

[63] J. D. Hunter, Comput. Sci. Eng. **9**, 90 (2007).

[64] S. Sugano, Y. Tanabe, and H. Kamimura, *Multiplets of Transition-Metal Ions in Crystals* (Academic Press, New York, 1970).